

Stray Light Correction and Enhancement of Nocturnal Low-Light Image of Early-Morning-Orbiting Fengyun-3E Satellite

Yongen Liang^{ID}, Min Min^{ID}, Hanlie Xu, Na Xu^{ID}, Danyu Qing, Xiuqing Hu^{ID}, Peng Zhang^{ID}, Senior Member, IEEE, Jing Li^{ID}, Xiaoxuan Mou^{ID}, and Zijing Liu

Abstract—The Chinese early-morning-orbiting Fengyun-3E (FY-3E) satellite fills the 6-h initial observation window for data assimilation in numerical weather prediction (NWP). The low-light band (LLB) on the medium-resolution spectral imager low light (MERSI-LL) of FY-3E can detect extremely low radiances at night, significantly enhancing nighttime observation capabilities as well as elevating data assimilation quality by improving the nighttime cloud mask algorithm. However, severe and nonlinear stray light contamination affects most nocturnal FY-3E/MERSI-LL LLB images, particularly those from the Southern Hemisphere, hindering further visualization applications. The analysis concluded that the stray light is closely associated with the refraction and reflection of sunlight entering the MERSI-LL, solar zenith angle (SZA), and detector number. To obtain clear and enhanced images, this study designed a fully automated and adaptive stray light correction and enhancement algorithm for the nocturnal low-light images of FY-3E/MERSI-LL. Three typical stray-light-contaminated scenarios were categorized for all nighttime images. The restored results showed that after processing, the “fog” stray light and stripes were essentially removed, and the details became richer and more prominent, significantly improving the visual effect and usability

Received 7 August 2024; revised 17 October 2024; accepted 14 November 2024. Date of publication 19 November 2024; date of current version 13 December 2024. This work was supported in part by the National Key Research and Development Program of China under Grant 2023YFF0805401, in part by the Natural Science Foundation of China under Grant 42175086, in part by the Innovation Group Project of Southern Marine Science and Engineering Guangdong Laboratory (Zhuhai) under Grant SML2023SP208, and in part by the Science and Technology Planning Project of Guangdong Province under Grant 2023B1212060019. The authors also acknowledge the high-performance computing support from the School of Atmospheric Science of Sun Yat-sen University. (*Corresponding author: Min Min.*)

Yongen Liang is with the School of Atmospheric Sciences, Southern Marine Science and Engineering Guangdong Laboratory (Zhuhai), Guangdong Province Key Laboratory for Climate Change and Natural Disaster Studies, Sun Yat-sen University, Zhuhai 519082, China, and also with the Department of Atmospheric and Oceanic Sciences, School of Physics, Peking University, Beijing 100081, China.

Min Min is with the School of Atmospheric Sciences, Southern Marine Science and Engineering Guangdong Laboratory (Zhuhai), Guangdong Province Key Laboratory for Climate Change and Natural Disaster Studies, Sun Yat-sen University, Zhuhai 519082, China (e-mail: minm5@mail.sysu.edu.cn).

Hanlie Xu, Na Xu, Danyu Qing, and Xiuqing Hu are with the National Meteorological Information Centre, China Meteorological Administration, Beijing 100081, China.

Peng Zhang is with the Meteorological Observation Center, China Meteorological Administration, Beijing 100081, China.

Jing Li is with the Department of Atmospheric and Oceanic Sciences, School of Physics, Peking University, Beijing 100081, China.

Xiaoxuan Mou is with Beijing Keytec Technology Company Ltd., Beijing 100081, China.

Zijing Liu is with Guangzhou Meteorological Satellite Ground Station, Guangzhou 510630, China.

Digital Object Identifier 10.1109/TGRS.2024.3502441

of the images. This algorithm is simple, efficient, and highly applicable, and will be integrated into the processing system of the FY-3E satellite to support near real-time applications of LLB images. However, some strong or unusual stray light still affects the local continuity of the images. Future low-light imagers of FY-3 satellites will feature more sophisticated instruments to reduce incident stray light in their optical system.

Index Terms—Early-morning-orbit, Fengyun-3E (FY-3E) satellite, image enhancement, low-light band (LLB), stray light correction.

I. INTRODUCTION

THE unique low-light optical sensor is primarily designed to detect extremely low radiances (ranging from 10^{-9} to $10^{-7} \text{ W}\cdot\text{m}^{-2}\cdot\text{s}^{r-1}$) emitted or reflected by the Earth's surface, such as nighttime airglow, city lights, and moonlight [1], [2]. In the early 1970s, the Operational Linescan System (OLS) was first deployed on the U.S. Defense Meteorological Satellite Program (DMSP) satellites to observe global low-light radiances at night [3]. In recent decades, the National Oceanic and Atmospheric Administration (NOAA) Suomi National Polar-orbiting Partnership Visible Infrared Imaging Radiometer Suite (S-NPP/VIIRS) DNB (referred to as the Day/Night Band) has become the most extensively used low-light sensor in the globe. It has generated various high-quality science and image products [4], which were freely and publicly released in 2012. Subsequently, the new-generation NOAA-20 and NOAA-21 polar-orbiting satellites were also equipped with similar VIIRS instruments to continue the night-time detection capabilities [5].

In DNB applications, the focus is primarily on radiance products. Due to the unique high-sensitivity detection capabilities of spaceborne low-light sensors, they have enabled a range of new applications in both natural and social science fields, providing a new perspective for observing the nocturnal Earth. Particularly, in the geoscience field, the use of spaceborne DNB data has enabled the development of new operational algorithms for satellites to retrieve cloud properties [6], [7], [8], detect clouds [9], [10], and uncover additional information about cloud layers and their physical mechanisms at night. Other studies have found that DNB's ability to capture faint glow from space allows it to observe the fine structure and evolution of atmospheric gravity waves [11], [12], significantly informing the description of gravity wave processes

in modeling schemes. With its advantages of high resolution and night vision, the low-light imager provides detailed information on typhoon eyewall positions, cloud structure, and wind shear during nighttime observations [13], aiding in the monitoring of typhoon dynamics and improving the timeliness and accuracy of warnings. It can observe the frequency and distribution of lightning and auroras at night, enhancing the understanding of thunderstorm characteristics and the effects of geomagnetic activity on the atmosphere [14]. Besides, DNB can also monitor nighttime lights, forest fires [15], aerosols [16], bioluminescent sea [17], and more. Among these, nighttime light products have become a key development area due to their significant social and economic benefits [18], [19]. The distribution and intensity changes of nighttime lights can reflect human activities, such as urbanization [20], fishing activities [14], and even wars [21].

Recently, China also developed and successfully launched an early-morning orbiting meteorological satellite on July 5, 2021, Fengyun-3E (FY-3E), equipped with a new low-light band (LLB) on the medium resolution spectral imager low light (MERSI-LL) [22]. Based on the FY-3E/MERSI-LL LLB observations, a new nighttime light product has been developed and applied [23]. However, other satellite remote sensing products are still undergoing testing and development due to severe stray light contamination in the low-light remote sensing images generated using pre-processed radiance data [see Fig. 1(c)–(f)]. These intractable issues in stray light contamination affect both image display and quantitative applications, particularly the observations during nighttime. Whereas, stray light contamination in nocturnal low-light images was also found in the previous S-NPP VIIRS/DNB. Scientists have developed a novel and robust correction algorithm to remove stray light in VIIRS/DNB images. Mills et al. [24] analyzed many contaminated VIIRS/DNB images and found that stray light depends on the detector number, scanning angle, solar zenith angle (SZA), and view geometries. They used the secondary fitting method in absolute dark scenes, the extrapolation method for dusk areas, and the quadruple fitting method for penumbral areas to effectively remove the stray light in the VIIRS/DNB images. Based on this algorithm, a monthly lookup table was regularly created for the S-NPP VIIRS/DNB data to treat stray light contamination offline operationally [25]. Subsequently, Lee et al. [26] designed a new method for online stray light correction based only on the gain ratio and dark offset of on-orbit calibrators, greatly improving the radiation correction effect for applications. Gu et al. [27] also corrected the error of the gain ratio based on linear regression, significantly reducing stripe contamination in VIIRS/DNB images due to detector nonlinearity.

Fig. 1 shows the typical stray-light-contaminated nighttime low-light remote sensing images observed by FY-3E/MERSI-LL LLB. Our investigation found that stray light in the nocturnal ($SZA > = 100^\circ$) FY-3E/MERSI-LL LLB images exhibits very strong nonlinear characteristics. Additionally, stray light is more severe and its types are more complex in nocturnal FY-3E/MERSI-LL LLB images of the Southern Hemisphere compared to the Northern Hemisphere, regardless of latitude. It can be reasonably inferred that this is primarily

due to the following factors: the high reflectivity of snow and ice in Antarctica, especially under bright moonlight, which increases the scattered light; more active auroral phenomena near the South Pole, creating additional brightness captured by LLB; differences in Earth's geomagnetic field, with the geomagnetic South Pole being closer to the geographic South Pole intensifying auroral activities; fewer artificial light sources in the Southern Hemisphere, making natural sources like moonlight and auroras more prominent; and the unique operational orbit and view geometries of FY-3E, causing stray light contamination more likely to occur in polar night regions of the Southern Hemisphere. Especially, a large number of FY-3E/MERSI-LL LLB images are contaminated by stray light, accounting for approximately 96.35% of the total samples at night (38 592 samples from March 2022 to May 2023). However, due to the unique nature of the early-morning-orbit and differences in instrument performance, the characteristics of stray light in FY-3E/MERSI-LL LLB images are significantly different from those in VIIRS/DNB stray-light-contaminated images [24]. The processing of FY-3E/MERSI-LL LLB images cannot directly adopt the sophisticated stray light correction algorithms developed and used for VIIRS/DNB. Therefore, the primary objective of this study is to develop a new image processing algorithm to adaptively and fully automatically correct stray light in FY-3E/MERSI-LL LLB images and ultimately restore clear images for data users. Note that, for this algorithm, it is necessary to consider the timeliness and robustness of real-time applications.

The organization of this article is as follows. Section II briefly introduces the FY-3E/MERSI-LL low-light data used in this study. Section III discusses the characteristics of stray light in FY-3E/MERSI-LL low-light remote sensing images. Section IV focuses on the algorithm and typical results of removing stray light and enhancing low-light images. Finally, this study concludes with a short summary in Section V.

II. DATA

FY-3E is the fifth polar-orbiting (sun-synchronous) meteorological satellite in the Chinese Fengyun-3 series and the world's first early-morning-orbit meteorological satellite for civil use. It was successfully launched on July 5, 2021. Its ascending node crossing time at the equator is 05:30 local standard time [28], providing observational data for the initial status of numerical models during dawn and dusk periods. The unique and innovative orbit design of FY-3E fills the 6-h initial observation window for data assimilation in numerical weather prediction (NWP) [29], thereby enhancing the accuracy of NWP forecasts.

The FY-3E satellite is equipped with 11 advanced instruments, among which the MERSI-LL is a crucial optical instrument. MERSI-LL has six infrared bands and an LLB, designed to provide high-precision quantitative retrieval of various science products, including nighttime lights, cloud masks, cloud top properties, land/sea surface temperatures, and more [22]. FY-3E/MERSI-LL LLB includes three types of gain channels: high gain (HGS), medium gain (MGS), and low gain (LGS). These channels are designed, respectively for low-visibility nighttime scenes, moderate-brightness twilight

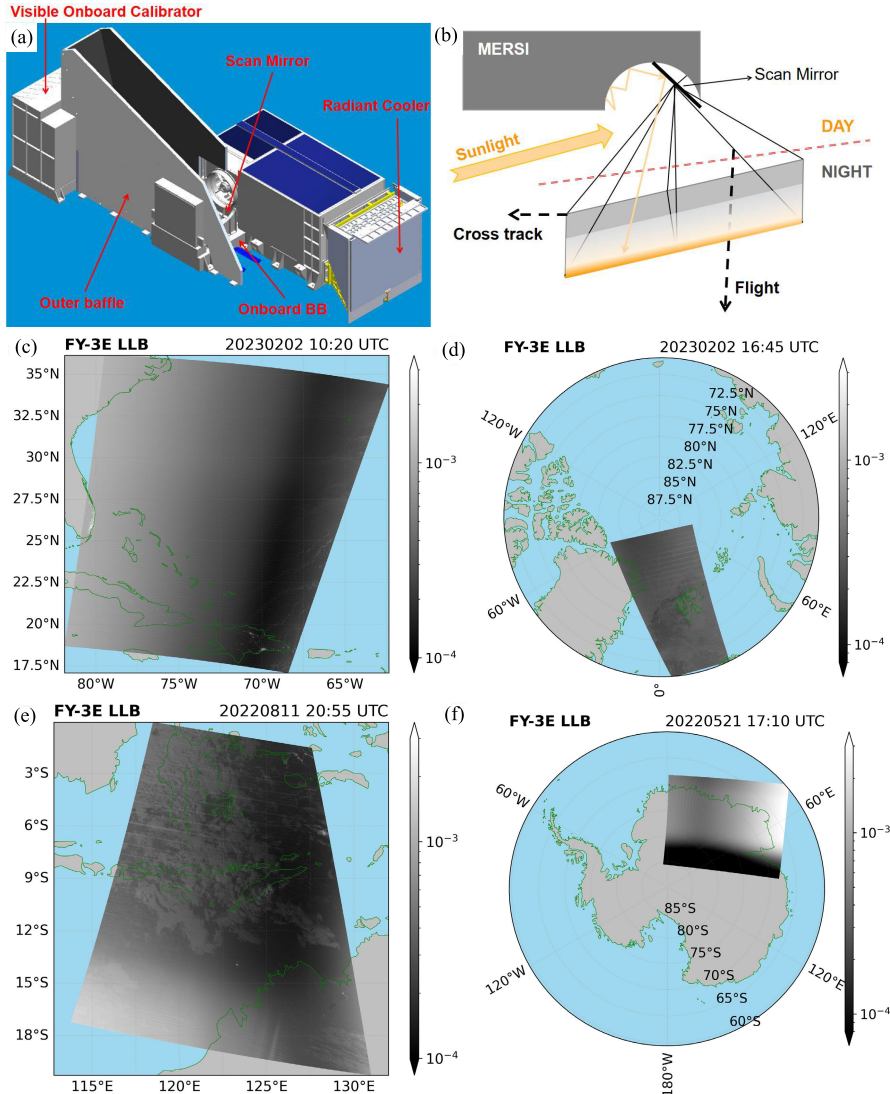


Fig. 1. (a) Schematic of the FY-3E/MERSI-LL instrument (from Hu et al. [30]). (b) Principle of stray light contamination caused by sunlight entering MERSI-LL and being reflected onto the LLB image through the scan mirror. (c)–(f) Stray-light-contaminated LLB image samples of FY-3E/MERSI-LL during nighttime for (c) low and (d) high latitudes in the Northern Hemisphere, as well as (e) low and (f) high latitudes in the Southern Hemisphere. The radiance values are plotted on a logarithmic scale to enhance image contrast and better observe details.

scenes, and high-brightness daytime scenes. This enables a wide dynamic range of earth target signal observation under lighting conditions ranging from one-quarter moonlight to sunlight, covering a radiance range of 3×10^{-5} – $90 \text{ W}\cdot\text{m}^{-2}\cdot\text{sr}^{-1}$ [30]. The spatial resolution of FY-3E/MERSI-LL LLB by the 10 detector elements scan mode is nominal 1000 m at nadir. In this investigation, we use the Level-1B (L1B) radiance data from the FY-3E/MERSI-LL to generate low-light images within a 5-min interval. Each L1B radiance data file has a grid size of 2000×1536 . For the LLB radiance matrix in each L1B file, the first seven columns and the last seven columns are invalid observations. Therefore, these invalid columns are removed from each matrix, leaving a valid matrix of size 2000×1522 .

III. CHARACTERISTICS OF STRAY LIGHT CONTAMINATION IN FY-3E LLB

As the previous study [23] has pointed out, the FY-3E satellite primarily passes through twilight zones or dawn bands, and

its nighttime observation range changes with the seasons. The sunlight will shine on the satellite body almost horizontally. This unique observation mode or geometry will inevitably introduce stray light from sunlight into the spaceborne optical sensors. In this study, we used FY-3E LLB data from March 2022 to May 2023 for analysis and research and ensured that nighttime aera had at least 30% coverage in full imagery.

Fig. 2 shows three typical scenarios of stray light contamination in FY-3E/MERSI-LL LLB images. The first scenario depicts the most common (the proportion is 91.13% of all nighttime images) type of stray light contamination [Fig. 2(a) and (b)]. It is evident that the stray light or bright “fog” area is located near the nighttime section on the left side. Generally, the stray light gradually weakens from the left side, where the SZA is the largest, to the right side of the image (the subfigures at the bottom panel of Fig. 2). Within the same scan line, the intensity of stray light decreases sharply as the SZA decreases, indicating a direct proportionality between stray light and SZA. However, the position of stray light in the

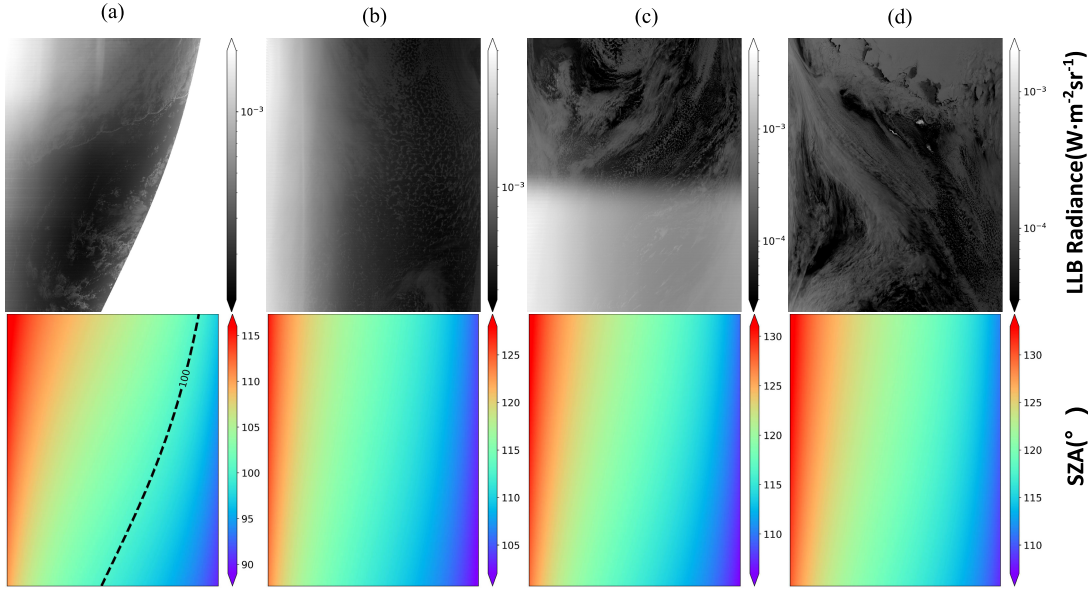


Fig. 2. FY-3E/MERSI-LL LLB nighttime radiance images (upper panel) and SZA maps (bottom panel). LLB radiance values are plotted with logarithmic grayscale. In subfigure a, the white part on the right-hand side at the upper panel represents the pixels with $SZA < 100^\circ$. (a) 20230511 13:00 UTC. (b) 20230507 12:45 UTC. (c) 20220714 13:10 UTC. (d) 20220613 19:45 UTC.

FY-3E LLB image is unpredictable and complex; sometimes it is mainly located in the left corner [e.g., Fig. 2(a)], while other times it covers almost the entire left side of the image [e.g., Fig. 2(b)]. Additionally, the intensity of the stray light exhibits periodic variations [30]. In some images, the stray light appears as a thin fog compared to the background, while in others it manifests as a strong glare [e.g., Fig. 2(a)]. Despite a sun-side baffle [Fig. 1(a)] being designed for suppressing stray light based on simulation experiments prior to launch [31], many low-light images still suffer from severe stray light contamination. The principle of stray light contamination in the LLB image can be specifically seen in Fig. 1(b). This is due to sunlight entering the scanning mirror cavity of MERSI-LL, where it refracts and reflects within the cavity, ultimately reflecting off the scanning mirror to create a bright spot on the imaging side near the night. The second scenario is the less common (the proportion is about 5.22% of all nighttime images) partial stray light type [Fig. 2(c)]. Its prominent feature is the stark contrast between extremely high and extremely low radiance values in the upper and lower parts of the image. There is no gradual transition zone in the middle; instead, a clear boundary separates the two levels of radiance. This boundary is approximately parallel to the horizontal scan lines. Yu et al. [23] also identified a similar light-dark boundary in the high latitudes of the Southern Hemisphere when analyzing the global radiance value trajectory of the FY-3E satellite. They explained that during the Southern Hemisphere winter, the FY-3E satellite is completely blocked by the Antarctic region, resulting in certain areas being free from incident light contamination. Thus, in a single image, the extremely low radiance values represent pure nighttime regions without stray light contamination, while the extremely high radiance values indicate areas with stray light contamination. This stark contrast in radiance values is magnified when plotted on a logarithmic scale. Besides, the characteristics of the stray light

contamination sub-regions are similar to those of the first type, suggesting that the processing method for the two types would be similar.

The third scenario consists of the few (the proportion is about 3.65% of all nighttime images) images completely free of stray light [Fig. 2(d)], which do not require additional processing for the “fog” stray light. It is similar to the cause of the second scenario. This type of image is captured in certain areas where FY-3E is completely obscured by the Antarctic region, so there is no incident light contamination at all. This only occurs near the Antarctic region. We also found that the second and third scenarios of images only appear in completely dark images at high latitudes in the Southern Hemisphere from April 17 to August 26, 2022, as well as April 17 to May 31, 2023.

It is worth noting that, as seen in the local magnified image (refer to Fig. 11 in the Appendix), all types of images with stray light contamination exhibit an inherent stripe feature throughout the entire image, indicating that stray light is also dependent on the detector number. Therefore, the upcoming work will focus on designing a fully automatic stray light correction and enhancement algorithm and evaluating its adaptability and effectiveness for these three main scenarios.

IV. STRAY LIGHT CORRECTION AND ENHANCEMENT ALGORITHM OF LOW-LIGHT IMAGE

A. Introduction on the Algorithm

As mentioned earlier, a significant proportion of images are affected by stray light contamination, approximately 96.35%, which severely impacts the application of FY-3E/MERSI-LL LLB images during nighttime. Therefore, a fast, adaptive, and fully automatic stray light correction and enhancement algorithm for low-light images is indispensable for the applications of FY-3E/MERSI-LL LLB images in meteorological

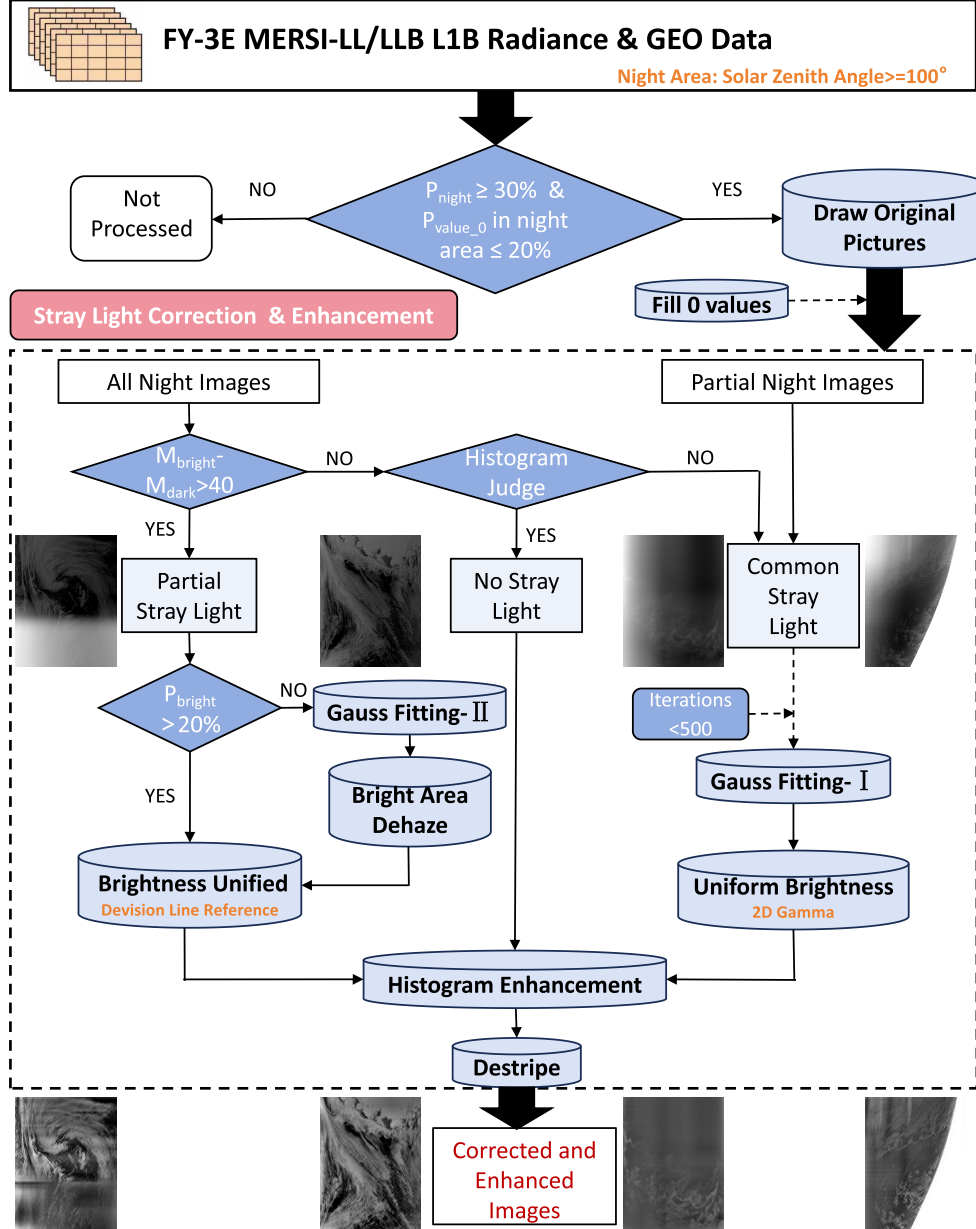


Fig. 3. Flowchart schematic of stray light correction and low-light image enhancement algorithm for FY-3E/MERSI-LL LLB. P_{night} and P_{value_0} in the night area, respectively, represent the proportion of the night area and the proportion of zero values within the night area in a single image. In a single LLB image of a partial stray light scenario, M_{bright} and M_{dark} , respectively, denote the average grayscale values in bright and dark areas, while P_{bright} represents the proportion of the bright area.

services. Both the timeliness and restoration quality of this automatic algorithm are prioritized and considered. Next, we will provide a detailed explanation and the flowchart of the processing steps of this fully automatic algorithm.

Fig. 3 illustrates the flowchart of the stray light correction and low-light image enhancement algorithm of FY-3E/MERSI-LL LLB developed in this study. We also discovered that some images exhibit abnormal radiance values of zero. To better display unambiguous images, we further selected samples with the proportion of zero values in the nighttime parts being less than or equal to 20% as an additional screening condition. In preprocessing, the test samples are plotted using a logarithmic scale to create the initial radiance images before

the algorithm is applied. If there are a few zero values in the image, use the bilinear interpolation method to fill in the zero values.

After the preprocessing step mentioned above, LLB images need to be categorized into three typical stray light contamination scenarios mentioned in Section III. First, the classification algorithm of the stray light contamination scenario will be performed as if all the pixels in the image are nocturnal, then enter the differentiation procedure to determine whether the no-stray light type or partial stray light type. If neither one meets the above two types, such complete night images are classified together with partial night images as universal stray light types with "fog" stray light.

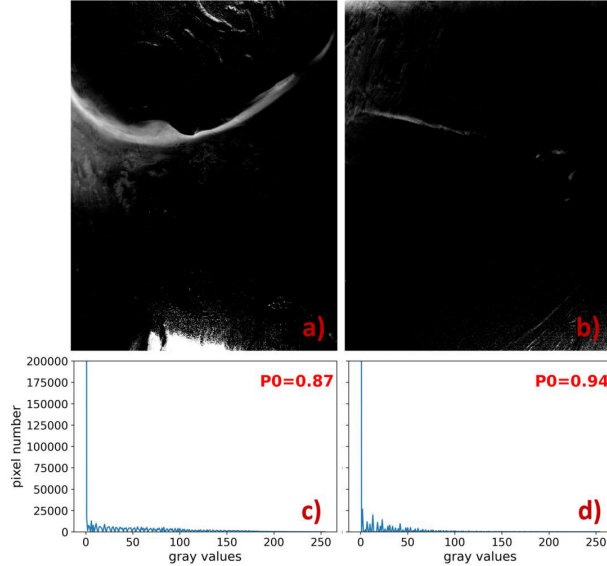


Fig. 4. FY-3E/MERSI-LL LLB radiance images (a) at 12:00 UTC on July 18, 2022, and (b) at 18:40 UTC on July 8, 2022. (c) and (d) Grayscale histograms of images (a) and (b), respectively, with 0 values filled, using an interval of 1 and a grayscale range of 0–254. P_0 in subfigures (c) and (d) represents the ratio of the frequency of 0 values to the total frequency of all grayscale values, rounded to two decimal places.

1) $M_{\text{bright}} - M_{\text{dark}} > 90$ Test: Due to the distinct differences in radiance values in partial stray light images, these images will be classified based on the significant difference in average grayscale values between the bright and dark areas. First, for each image, the classical Otsu [32] is applied to calculate the adaptive threshold for binarization segmentation of the entire LLB image. Next, the row where the difference between the threshold and the average grayscale value of the row is minimal is selected as the horizontal segmentation line for this study. Finally, if the average grayscale value of the bright region (M_{bright}) differs from that of the dark region (M_{dark}) by more than 90, the image is categorized as a partial stray light type. This is because, for this type of image, the binarization segmentation threshold is very close to the average grayscale value at the boundary between the bright and dark regions.

2) Histogram Judge Test: This test, which is executed if step (1) fails, aims to extract images without stray light contamination. The histogram image represents a typical frequency distribution of grayscale levels, effectively converting the complex 2-D image matrix into usable 1-D statistical data.

First, for dark images with few objects and no stray light [e.g., Fig. 4(a) and (b)], most areas have low grayscale values. Their histograms [Fig. 4(c) and (d)] show a high frequency of zero values. An empirical condition is set where the zero-value frequency proportion is ≥ 0.85 .

Second, bright images without stray light [e.g., Fig. 5(a)] have uniform brightness and a narrow peak in the histogram [Fig. 5(d)]. We design an algorithm that from the sliding fitting on the histogram curve, a significant narrow peak that meets the condition of its significance (SF) $> 80\,000$, is identified with no other prominent peaks. For images with stray light [e.g., Fig. 5(b)], the right width of the narrow peak at 95th

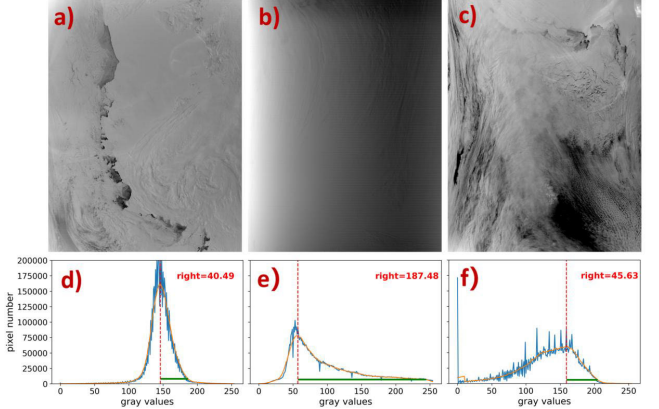


Fig. 5. Same as Fig. 4, but for the FY-3E/MERSI-LL LLB radiance images (a) at 11:35 UTC on May 17, 2022, (b) at 12:00 UTC on May 16, 2022, and (c) at 00:00 UTC on July 13, 2022. (d)–(f) Are the grayscale histograms of images (a)–(c), respectively. The blue solid line represents the grayscale histogram curve, and the orange line represents the sliding fitting of the histogram curve. “right” indicates the right peak width at the 95th percentile.

percentile of the peak height is longer [Fig. 5(e)]. So another restrictive condition is set that this width is < 90 .

Finally, for dark images with more objects and no stray light [e.g., Fig. 5(c)], the fitting lines [Fig. 5(f)] have a lower peak and higher curvature. Images are identified from the fitting line, by a peak with SF $< 80\,000$, the right peak width at 95th percentile < 90 , and the number of peaks and troughs with SF $> 15\,000$ (seen as curvature) ≥ 10 .

To test this identification approach, 100 images were randomly selected from the complete night images and two groups were tested independently. From the experimental results (https://zenodo.org/records/13195689/validate_Histogram_Judge_Test.rar), we found that this method has achieved a very good discrimination effect.

3) Gauss Fitting-I Algorithm: From Fig. 3, after the accurate classification of LLB images based on the two tests mentioned before (partial stray light, no stray light, and common stray light), the subsequent stray light correction algorithm will be executed according to their characteristics following different procedures. The next steps for correcting the common stray light contamination in LLB images are as follows.

Since the strength of “fog” stray light in the image generally exhibits an exponential decrease, and the profile of the stray light is relatively smooth, resembling the edges of a circle or ellipse, it shares characteristics with Gaussian blobs. Therefore, we chose to fit the stray light contamination with a 2-D Gaussian function [33], which is expressed as follows:

$$\text{Gauss}(x, y) = a \times e^{-\left[\frac{(x-x_0)^2}{2\sigma_x^2} + \frac{(y-y_0)^2}{2\sigma_y^2}\right]} \quad (1)$$

where a represents the peak amplitude. x_0 and y_0 , respectively, denote the center position of the 2-D Gaussian spot. σ_x and σ_y are the standard deviations in the x - and y -directions, respectively.

The specific implementation method is as follows: first, use the 50th percentile of the nighttime L1B radiance values as an estimate of the background radiance value (BRV). Then,

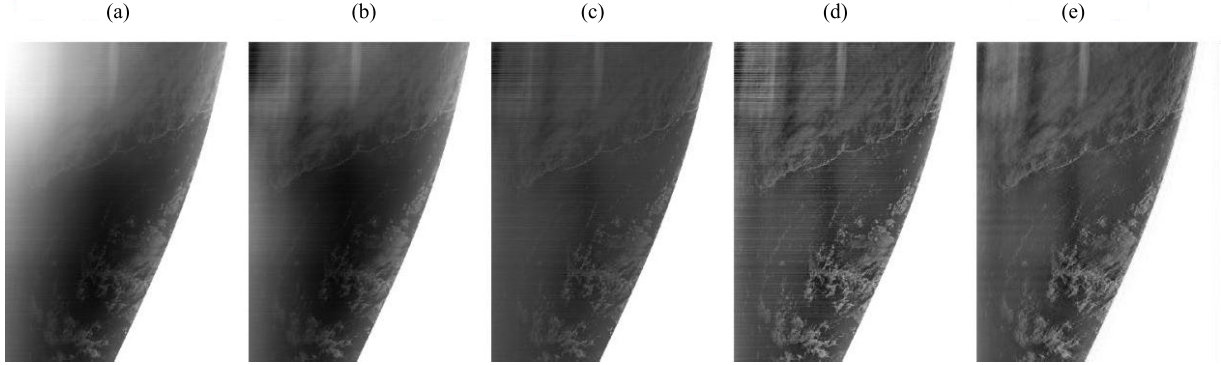


Fig. 6. Restoration effects of Gaussian fitting, brightness equalization, enhancement, and stripes removal for FY-3E/MERSI-LL nighttime LLB images contaminated by stray light at 13:00 UTC on May 11, 2023. (a) Original LLB. (b) Gauss fitting. (c) Uniform brightness. (d) Enhance. (e) Destripe.

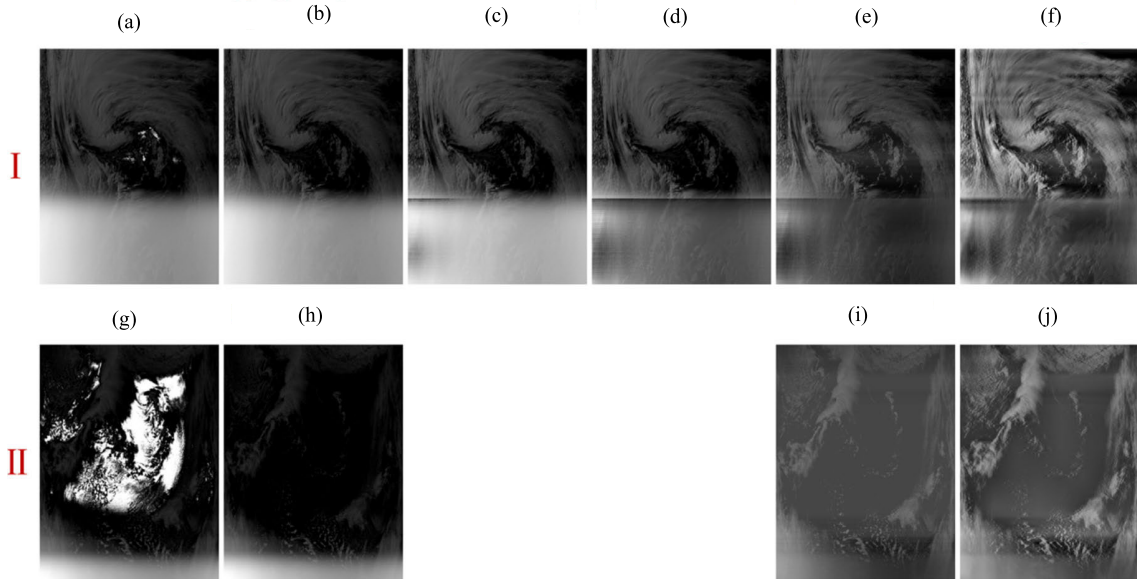


Fig. 7. (Top panel or Row-I) Restoration effects of each step including filling in 0 values, Gaussian fitting, haze removal from the bright area, brightness uniformity, enhancement, and stripe removal on the LLB images at 16:20 UTC on June 13, 2022. (Bottom panel or Row-II) Restoration effects of each step including filling in 0 values, enhancement, and stripe removal on the LLB images at 14:45 UTC on June 18, 2022. (a) Original LLB. (b) Fill 0 values. (c) Gauss fitting. (d) Bright area Dehaze. (e) Brightness unified. (f) Enhance & Destripe. (g) Original LLB. (h) Fill 0 values. (i) Brightness unified. (j) Enhance & Destripe.

subtract BRV from the radiance values that are greater than BRV, and apply the nonlinear least squares fitting using (1). Finally, subtract the fitting function from all the original radiance values to obtain the corrected image [Fig. 6(b)]. It can be seen that the strong stray light in Fig. 6(a) is eliminated, and, in contrast, the corrected image [Fig. 6(b)] does not show obvious transition areas. In addition, most images have a fast fitting speed (2–5 s), further validating the feasibility of this function.

However, for a small portion of images where the “fog” scatter light is more complex (e.g., with sharp edges), which deviates significantly from characteristics of Gaussian blobs, the fitting iteration time is very long. Due to operational speed requirements, the number of iterations is set to no more than 500. If optimal parameters are not achieved within 500 iterations, the 70th, 80th, and 90th percentiles of nighttime radiance values will be treated as BRV in sequence. If the fitting is still unsuccessful within 500 iterations, the fitting

is abandoned, and the process moves directly to the next correction step.

4) Uniform Brightness Algorithm: Although the main strong stray light has been removed in Fig. 6(b), weak light can still be visually detected in the left and upper-left corners of the image, causing uneven brightness distribution in the LLB image. To address this issue, we use the image adaptive illumination correction algorithm proposed by Liu et al. [34]. The principle of this algorithm is to obtain the illumination component and then apply a 2-D gamma function to adjust the brightness of the V component in the HSV color space of the original image. The result of the algorithm is shown in Fig. 6(c), where the brightness is more uniform and the cloud features in the image remain not much different, without significant blurring compared to the original image.

5) Histogram Enhancement Algorithm: To further elevate and emphasize the clarity and distinctiveness of objects in LLB images, Contrast Limited Adaptive Histogram Equalization

TABLE I
PURPOSES AND CRITICAL THRESHOLDS OF THE TESTS AND ALGORITHMS IN THE STRAY LIGHT CORRECTION AND ENHANCEMENT ALGORITHM

No.	Test / Algorithm	Purpose	Critical Threshold
1	$M_{\text{bright}} - M_{\text{dark}} > 90$	Determine whether it is a partial stray light scenario	90
2	Histogram Judge	Determine whether it is a non-stray-light scenario	(1) $P_0 \geq 0.85$ OR (2) Only one prominent peak($SF > 80,000$) & right < 90 OR (3) A peak ($SF < 80,000$) & right < 90 & N(peaks and troughs, $SF > 15,000$) < 100
3	Gauss Fitting-I	Remove "fog" stray light in common stray light scenario	$BRV = 50^{\text{th}}$ ($70^{\text{th}}, 80^{\text{th}}, 90^{\text{th}}$ if iterations > 500) radiance
4	Uniform Brightness	Make the brightness more uniform in common stray light scenario	—
5	Histogram Enhancement	Make objects more visually distinct and recognizable	The contrast limit factor=2.0
6	Destripe	Remove the stripes	(1) The highest decomposition level = 5 AND (2) The damping factor for the Fourier transform = 10
7	Gauss Fitting-	Remove "fog" stray light in partial stray light scenario (the bright area exceeds 0.2)	(1) 30^{th} radiance as a threshold to remove radiation values without stray light AND (2) $BRV = 80^{\text{th}}$ remaining radiance
8	Bright Area Dehaze	Remove the haze stray light in the bright area in partial stray light scenario (the bright area exceeds 0.2)	Window size=15, Transmission regulation factor=0.8, Transmission map threshold=0.1
9	Brightness Unified	Make the brightness more uniform and weaken the transition line in partial stray light scenario	Reference value(R) = $\begin{cases} R, R < 80 \\ R - 30, 80 \leq R < 120 \\ R - 50, 120 \leq R \end{cases}$

Notes: P_0 , SF, right, BRV represent the ratio of the frequency of 0 values to the total frequency of all grayscale values, the significance of the peak/trough, the right peak width at the 95th percentile and the Background Radiance Value, respectively.

(CLAHE) [35] was introduced to improve image contrast. In this study, the contrast limit factor was set to 2.0. The results indicate that, the enhanced image [Fig. 6(d)] is visually clearer compared to Fig. 6(c). The application of CLAHE significantly improves the visibility of the edges and fine textures of the clouds, giving the cloud layers a more stereoscopic appearance. This enhancement reveals additional details and complex structures within the clouds, highlighting the valid information on LLB images.

However, it can introduce local block artifacts (specific regions may appear overly bright or dark). Additionally, residual noise in the image is often amplified, particularly in uniform areas, which can create unwanted artifacts or even obscure important details. The overall brightness

of the image might also change noticeably compared to the original.

6) *Destripe Algorithm:* After the enhancement process, the inherent stripes (induced by the vibration of the microwave sensor on the same FY-3E satellite platform) in the original image also become more prominent, and it is observed that the intensity and pattern of these stripes are consistent throughout the image. After trying various classical algorithms, the optimal performance is achieved using the stripe removal algorithm proposed by Münch et al. [36], which combines wavelet transform and Fourier filtering analysis. This algorithm is advantageous because it is stable, effective, and speedy. For LLB images, the wavelet type chosen is the bior5.5 from the Biorthogonal wavelets (abbreviated as

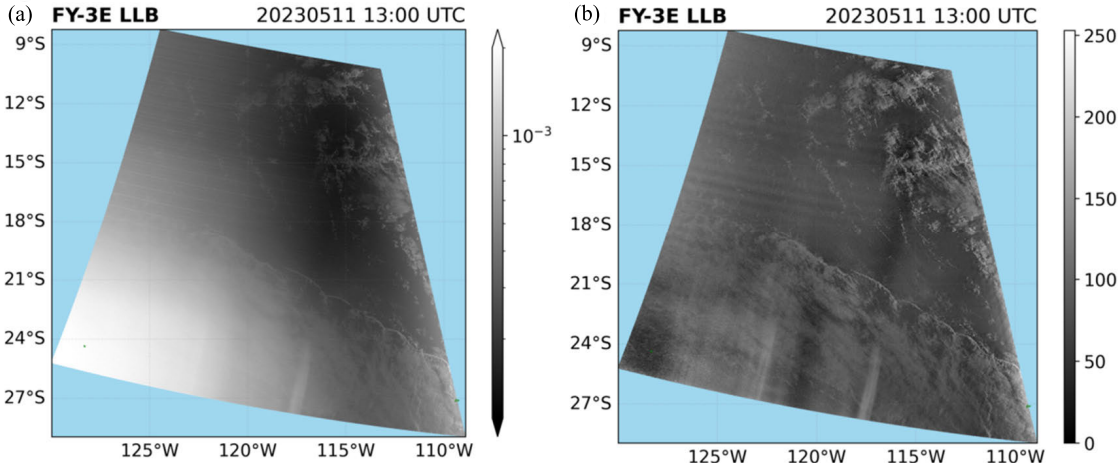


Fig. 8. Comparison between (a) original FY-3E/MERSI-LL LLB nighttime radiance image and (b) clear image after algorithm processing at 13:00 UTC on May 11, 2023.

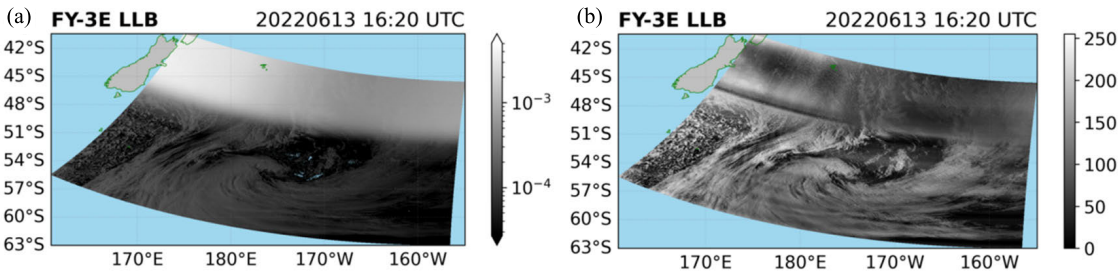


Fig. 9. Same as Fig. 8, but the sample at 16:20 UTC on June 13, 2022.

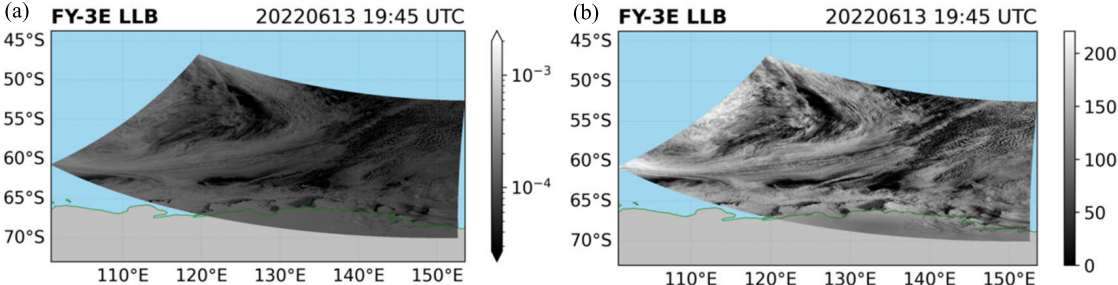


Fig. 10. Same as Fig. 8, but the sample at 19:45 UTC on June 13, 2022.

bior). Compared to other wavelets, its filters are symmetric, effectively removing noise while preserving the edges and details of LLB images during reconstruction [37], [38].

Moreover, based on multiple parameter experiments, the two key parameters best suited for Fig. 6(d) were determined: the highest decomposition level = 5 and the damping factor for the Fourier transform = 10. These parameters also perfectly and accurately apply to all other LLB images. The result of this algorithm is shown in Fig. 6(e), where the inherent horizontal stripes have been completely removed, yielding a final clear image. However, filtering specific frequencies can overly smooth high-frequency details like edges and textures, leading to detail loss. Furthermore, combining the wavelet and Fourier transforms requires careful handling of domain conversions, as errors during the inverse transformation can distort the image's geometry or brightness distribution.

Using Fig. 7 as an example, the following sections will describe the steps for processing images of partial stray light scenarios (see Fig. 3).

7) *Gauss Fitting-II Algorithm:* After filling the zero values, if the bright area exceeds 0.2 (Row I), the stray light in the bright area also needs to be processed with Gaussian fitting. The principle is the same as the Gauss Fitting-I Algorithm mentioned above. Due to the presence of an extremely dark area without stray light, the background value has been modified in the processing. First, we use the 30th percentile of all L1B radiation values as the threshold to remove radiation values without stray light. Then, we estimate the BRV using the 80th percentile of the remaining radiation values, followed by subsequent Gaussian fitting steps. It is important to note that the correction is limited to the bright area defined by the method in step (2). Remarkably, practical results show that

under this scenario, fitting can be quickly achieved, thus there is no need to adjust the BSV. The processed image is shown in Fig. 7(c), where it can be seen that the prominent bright spot on the left side of the bright area has been removed.

8) *Bright Area Dehaze Algorithm*: As introduced before, step (7) makes the stray light contamination in the bright area relatively more uniform. Based on this characteristic, we applied the classical dark channel prior dehazing algorithm [39] to the bright area. This algorithm is based on the atmospheric scattering model. The result is shown in Fig. 7(d), where most of the haze stray light contamination is removed from the bright area, revealing effective information such as the texture and structure of the clouds.

9) *Brightness Unified Algorithm*: The bright area, after processing, has a visible transition line with the dark area, which, if left untreated, will become more prominent in the subsequent enhancement and increase image noise. Therefore, we have designed a simple algorithm: for the row where the transition line found by the OTSU method is located, we calculate the average grayscale value of that row as a reference value. Then, the difference between the average grayscale value of each row in the image and the reference value is used as the correction value for each pixel in that row. If the reference value is too large, it will be reduced to ensure that the final image is not too bright. As a result, the transition line is successfully weakened, and the overall brightness distribution of the image becomes much more uniform [Fig. 7(e)].

Additionally, for images where the bright area proportion does not exceed 0.2 (Row II), the sample size of the bright spot is too small, resulting in poor performance in Gaussian fitting. Therefore, for these images, steps (7)–(8) are skipped, and brightness uniformity is applied directly. As shown in Fig. 7(i), the stray light at the bottom of the image is completely removed, and there is almost no trace of the transition line.

After the above operations, the process moves on to the enhancement (5) and destriping (6) steps, ultimately resulting in a clear, stray light-free image [Fig. 7(f) and (j)]. For the third scenario of LLB images, which is free of stray light, no additional operations are needed; simply performing steps (5) and (6) will yield a usable and clear image. Table I summarizes the primary purposes of the above methods and their key application thresholds.

B. Results and Discussion

The proposed algorithm in Section IV-A was successfully and automatically applied to all samples of FY-3E/MERSI-LL LLB under the three previously mentioned stray-light-contaminated scenarios. The typical results are shown in Figs. 8–10.

Fig. 8 illustrates the correction effect for the first common stray light scenario. After processing, it is evident that the significant stray light is completely removed, revealing the cloud textures and structures previously obscured by the “fog” of stray light, thus providing more useful information. In Fig. 8(b), the boundary of the originally strong stray light area becomes smoother. Overall, the visual quality of the image has significantly improved, with details being clearer

and more prominent than in Fig. 8(a). This enhancement will be valuable in practical applications such as weather analysis and activity assessment. However, there are two unevenly bright coarse bands at the bottom of the image, the cause of which has not yet been determined. These light bands are more localized than other stray light, rendering the Gaussian fitting algorithm ineffective in removing them. Additionally, there is a wider stripe in the middle of the left side of Fig. 8(a).

Similar to Figs. 8 and 9, this represents the result of the second scenario of LLB images with partial stray light. Compared to Fig. 8, due to the limitations of the image characteristics, some stray light and the transition line remain in the processed image. However, the image restoration has achieved the best possible results. In the bright area, the middle and right parts, which are far from the strongest stray light, show clearer cloud structures and maintain continuous connections with the cloud structures in the dark area. The correction effect at the strongest stray light position (left end) is slightly inferior.

In contrast, Fig. 10 shows the result of the third scenario of the LLB image without stray light. It demonstrates that the algorithm not only highlights the features and textures of the clouds but also preserves the spatial structural characteristics of the original information.

The primary objective of FY-3E/MERSI-LL LLB in business operations is to quickly and stably produce clear images, not to re-calibrate observed radiance during nighttime. Therefore, the evaluation of the product is not merely an error analysis. Although the stray light correction is not perfect, it has nearly eliminated all stray light in the images, significantly improving the image quality and visual effect. Additionally, the algorithm designed in this article is very efficient, greatly saving computational resources and memory, thus meeting business requirements and operational applications. Most importantly, the algorithm has demonstrated strong robustness and stability, showing good correction effects for almost all samples. In the future, it will also be integrated into the processing system of FY-3E/MERSI-LL for near real-time operational applications at the National Satellite Meteorological Center, China Meteorological Administration. For detailed information and more results from this algorithm, please refer to the <https://zenodo.org/records/13195689>.

V. SUMMARY AND CONCLUSION

In this investigation, we analyzed the characteristics and sources of stray light in the nocturnal LLB images from MERSI-LL onboard early-morning-orbiting FY-3E satellite. After that, we designed a fully automated and adaptive stray light correction and enhancement algorithm to obtain clear images for endorsing near real-time operational applications of LLB images during nighttime. The stray light in FY-3E/MERSI-LL LLB images exhibits significant nonlinear characteristics, with more severe pollution in the samples in the Southern Hemisphere compared to the Northern Hemisphere. The stray light can be categorized into three typical scenarios: common stray light, partial stray light, and no stray light. Furthermore, the analysis indicates that the stray light is related to the refraction and reflection of sunlight

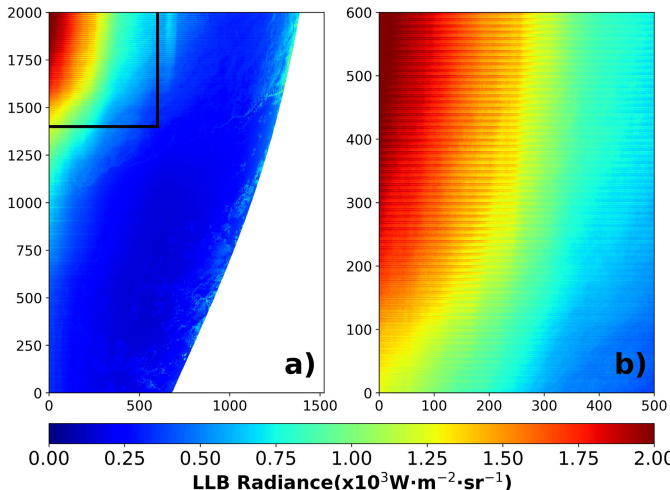


Fig. 11. (a) LLB radiance map of Fig. 2(a). (b) Related zoomed area within the black box in subfigure (a), both plotted using the same normalized jet scale.

entering the MERSI-LL instrument, SZA, and the detector number of MERSI-LL/LLB. However, due to the uniqueness and complexity of stray light in this instrument, traditional methods cannot be directly employed to correct stray light and enhance the image.

To restore and enhance LLB images during nighttime as much as possible, the algorithm designed in this article first distinguishes among the three typical scenarios, then selects the appropriate method for on-orbit stray light correction and enhancement of FY-3E/MERSI-LL LLB images. The results show that after processing, the “fog” stray light and stripes are removed, and the details are richer and more prominent, significantly improving the visual effect and usability of the images. This method is simple, efficient, and highly applicable. All nighttime samples from March 2022 to May 2023 have been tested.

However, some strong or unusual stray light still affects the local continuity of the images, which will motivate further research and refinement. In the future, more advanced technologies will be designed and applied to suppress on-orbit stray light contamination in the low-light images of the Fengyun-3 or Fengyun-5 series polar-orbiting meteorological satellites.

ACKNOWLEDGMENT

The authors would like to acknowledge NOAA for freely. The authors would like to express their gratitude to the authors and contributors of the online algorithms and resources that significantly aided their research. Specifically, They acknowledge the following resources: Uniform Brightness Algorithm, https://blog.51cto.com/u_13984132/5617762; Destripe Algorithm available at <https://github.com/DHI-GRAS/rmstripes>; Dark Channel Prior dehazing algorithm at <https://blog.csdn.net/leviopku/article/details/83898619>. These resources provided invaluable support in the development and implementation of their methodologies. Finally, They would also like to thank the editor and anonymous reviewers for their thoughtful suggestions and comments.

DATA AVAILABILITY STATEMENT

Fengyun-3E satellite data used in this study are freely downloaded from the official website of National Satellite Meteorological Center, CMA at <http://satellite.nsdc.org.cn/PortalSite/Data/DataView.aspx?currentculture=en-US>. Satellite imageries and codes in this investigation are available from <https://zenodo.org/records/13195689>.

APPENDIX

See Fig. 11.

REFERENCES

- [1] E. C. Stokes et al., “Retired satellites: A chance to shed light,” *Science*, vol. 373, no. 6562, pp. 1451–1452, Sep. 2021.
- [2] M. Min et al., “A low-light radiative transfer model for satellite observations of moonlight and Earth surface light at night,” *J. Quant. Spectrosc. Radiat. Transf.*, vol. 247, May 2020, Art. no. 106954.
- [3] T. A. Croft, “Nighttime images of the Earth from space,” *Scientific Amer.*, vol. 239, no. 1, pp. 86–98, Jul. 1978.
- [4] M. O. Román et al., “NASA’s black marble nighttime lights product suite,” *Remote Sens. Environ.*, vol. 210, pp. 113–143, Jun. 2018.
- [5] C. Cao, F. J. De Luccia, X. Xiong, R. Wolfe, and F. Weng, “Early on-orbit performance of the visible infrared imaging radiometer suite onboard the Suomi national polar-orbiting partnership (S-NPP) satellite,” *IEEE Trans. Geosci. Remote Sens.*, vol. 52, no. 2, pp. 1142–1156, Feb. 2014.
- [6] M. Min et al., “An investigation of the implications of lunar illumination spectral changes for day/night band-based cloud property retrieval due to lunar phase transition,” *J. Geophys. Res., Atmos.*, vol. 122, no. 17, pp. 9233–9244, Sep. 2017.
- [7] M. Min, L. Zhang, P. Zhang, and Z. Yao, “Can the Earth–Moon distance influence the accuracy of lunar irradiance with the plane-parallel assumption in atmospheric radiative transfer at night?” *J. Atmos. Sci.*, vol. 78, no. 8, pp. 2459–2469, Aug. 2021.
- [8] A. Walther, A. K. Heidinger, and S. Miller, “The expected performance of cloud optical and microphysical properties derived from suomi NPP VIIRS day/night band lunar reflectance,” *J. Geophys. Res., Atmos.*, vol. 118, no. 23, p. 13, Dec. 2013.
- [9] S. D. Miller et al., “A physical basis for the overstatement of low clouds at night by conventional satellite infrared-based imaging radiometer bi-spectral techniques,” *Earth Space Sci.*, vol. 9, no. 2, Feb. 2022, Art. no. e2021EA00213.
- [10] L. Sun et al., “A cloud detection algorithm-generating method for remote sensing data at visible to short-wave infrared wavelengths,” *ISPRS J. Photogram. Remote Sens.*, vol. 124, pp. 70–88, Feb. 2017.
- [11] S. D. Miller et al., “The dark side of hurricane Matthew: Unique perspectives from the VIIRS day/night band,” *Bull. Amer. Meteorological Soc.*, vol. 99, no. 12, pp. 2561–2574, Dec. 2018.
- [12] C. Lai, J. Yue, J. Xu, W. C. Straka, S. D. Miller, and X. Liu, “Suomi NPP VIIRS/DNB imagery of nightglow gravity waves from various sources over China,” *Adv. Space Res.*, vol. 59, no. 8, pp. 1951–1961, Apr. 2017.
- [13] J. D. Hawkins et al., “Tropical cyclone characterization via nocturnal low-light visible illumination,” *Bull. Amer. Meteorological Soc.*, vol. 98, no. 11, pp. 2351–2365, Nov. 2017.
- [14] S. Miller et al., “Illuminating the capabilities of the Suomi national polar-orbiting partnership (NPP) visible infrared imaging radiometer suite (VIIRS) day/night band,” *Remote Sens.*, vol. 5, no. 12, pp. 6717–6766, Dec. 2013.
- [15] I. Csizar et al., “Active fires from the suomi NPP visible infrared imaging radiometer suite: Product status and first evaluation results,” *J. Geophys. Res., Atmos.*, vol. 119, no. 2, pp. 803–816, Jan. 2014.
- [16] J. Wang et al., “Development of a nighttime shortwave radiative transfer model for remote sensing of nocturnal aerosols and fires from VIIRS,” *Remote Sens. Environ.*, vol. 241, May 2020, Art. no. 111727.
- [17] S. D. Miller, “Boat encounter with the 2019 Java bioluminescent milky sea: Views from on-deck confirm satellite detection,” *Proc. Nat. Acad. Sci. USA*, vol. 119, no. 29, pp. –9, Jul. 2022, Art. no. e220761211.
- [18] N. Levin et al., “Remote sensing of night lights: A review and an outlook for the future,” *Remote Sens. Environ.*, vol. 237, Feb. 2020, Art. no. 111443.
- [19] S. D. Miller, S. P. Mills, C. D. Elvidge, D. T. Lindsey, T. F. Lee, and J. D. Hawkins, “Suomi satellite brings to light a unique frontier of nighttime environmental sensing capabilities,” *Proc. Nat. Acad. Sci. USA*, vol. 109, no. 39, pp. 15706–15711, Sep. 2012.

- [20] Q. Zheng, K. C. Seto, Y. Zhou, S. You, and Q. Weng, "Nighttime light remote sensing for urban applications: Progress, challenges, and prospects," *ISPRS J. Photogramm. Remote Sens.*, vol. 202, pp. 125–141, Aug. 2023.
- [21] X. Li, S. Liu, M. Jendryke, D. Li, and C. Wu, "Night-time light dynamics during the Iraqi civil war," *Remote Sens.*, vol. 10, no. 6, p. 858, Jun. 2018.
- [22] P. Zhang et al., "The on-orbit performance of FY-3E in an early morning orbit," *Bull. Amer. Meteorological Soc.*, vol. 105, no. 1, pp. E144–E175, Jan. 2024.
- [23] T. Yu, L. Chen, N. Xu, H. Xu, X. Hu, and X. Zhang, "Fengyun-3E low light observation and nighttime lights product," *IEEE Trans. Geosci. Remote Sens.*, vol. 61, 2023, Art. no. 4703612.
- [24] S. Mills, S. Weiss, and C. Liang, "VIIRS day/night band (DNB) stray light characterization and correction," in *Proc. SPIE*, 2013, pp. 549–566.
- [25] L. B. Liao, S. Weiss, S. Mills, and B. Hauss, "Suomi NPP VIIRS day-night band on-orbit performance," *J. Geophys. Res., Atmos.*, vol. 118, no. 22, p. 12, Nov. 2013.
- [26] S. Lee, J. McIntire, H. Oudrari, T. Schwarting, and X. Xiong, "A new method for suomi-NPP VIIRS day–night band on-orbit radiometric calibration," *IEEE Trans. Geosci. Remote Sens.*, vol. 53, no. 1, pp. 324–334, Jan. 2015.
- [27] Y. Gu, S. Upadhyay, S. Blonski, B. Zhang, and C. Cao, "Improved algorithm for determining the visible infrared imaging radiometer suite day/night band high-gain stage dark offset free from light contamination," *Appl. Opt.*, vol. 58, no. 6, p. 1400, 2019.
- [28] P. Zhang et al., "FY-3E: The first operational meteorological satellite mission in an early morning orbit," *Adv. Atmos. Sci.*, vol. 39, no. 1, pp. 1–8, Jan. 2022.
- [29] P. Zhang et al., "Latest progress of the Chinese meteorological Satellite program and core data processing technologies," *Adv. Atmos. Sci.*, vol. 36, no. 9, pp. 1027–1045, Sep. 2019.
- [30] X. Hu et al., "Overview of low light detection and application of FY-3 early morning satellite," *Acta Optica Sinica*, vol. 42, pp. 41–54, Jun. 2022.
- [31] H. Chen et al., "Effect of external stray light on low-light imager loaded in Fengyun-3 day/night orbit meteorological Satellite," *Laser Optoelectronics Prog.*, vol. 54, pp. 103–108, 2017.
- [32] N. Otsu, "A threshold selection method from gray-level histograms," *Automatica*, vol. 11, nos. 285–296, pp. 23–27, 1975.
- [33] C. B. Do, "The multivariate Gaussian distribution," in *Proc. Sect. Notes, Lect. Mach. Learn., CS*, vol. 229, 2008.
- [34] Z. C. Liu, D. W. Wang, Y. Liu, and X. J. Liu, "Adaptive adjustment algorithm for non-uniform illumination images based on 2D gamma function," *Trans. Beijing Inst. Tec.*, vol. 36, no. 2, pp. 191–196, Nov. 2016.
- [35] S. M. Pizer et al., "Adaptive histogram equalization and its variations," *Comput. Vis., Graph., Image Process.*, vol. 39, no. 3, pp. 355–368, Sep. 1987.
- [36] B. Münch, P. Trtik, F. Marone, and M. Stampanoni, "Stripe and ring artifact removal with combined wavelet-Fourier filtering," *Opt. Exp.*, vol. 17, no. 10, pp. 8567–8591, 2009.
- [37] J. Zhang, Q. Zhu, and L. Song, "Wavelet-based self-adaptive hierarchical thresholding algorithm and its application in image denoising," *Traitemet du Signal*, vol. 36, no. 6, pp. 539–547, Dec. 2019.
- [38] S. Wang et al., "Wavelet entropy and directed acyclic graph support vector machine for detection of patients with unilateral hearing loss in MRI scanning," *Frontiers Comput. Neurosci.*, vol. 10, p. 106, Oct. 2016.
- [39] K. He, J. Sun, and X. Tang, "Single image haze removal using dark channel prior," *IEEE Trans. Pattern Anal. Mach. Intell.*, vol. 33, no. 12, pp. 2341–2353, Dec. 2010.



Yongen Liang received the B.S. degree in atmospheric meteorology from the School of Atmospheric Sciences, Sun Yat-sen University, Zhuhai, China, in 2024. She is currently pursuing the Ph.D. degree with the Department of Atmospheric and Oceanic Sciences, School of Physics, Peking University, Beijing, China.

Her research interests include cloud and weather satellite remote sensing and cloud physics.



Min Min received the B.S. degree in applied meteorology from the Nanjing University of Information Science and Technology, Nanjing, China, in 2005, and the Ph.D. degree in atmospheric physics and environment from the Chinese Academy of Sciences, Beijing, China, in 2010.

From 2010 to 2019, he worked with the National Satellite and Meteorological Center, China Meteorological Administration (NSMC/CMA), Beijing. From 2013 to 2014, he was a Visiting Research Assistant with the Department of Physics, University

of Maryland at Baltimore County (UMBC), Baltimore, MD, USA. He is currently a Professor with the School of Atmospheric Sciences, Sun Yat-sen University, Zhuhai, China. His research interests include cloud and weather satellite remote sensing, atmospheric radiative transfer, and calibration of satellite sensors.



Hanlie Xu received the B.S. degree in atmospheric science from the Nanjing University of Information Science and Technology, Nanjing, Jiangsu, China, in 2008, and the Ph.D. degree in meteorology from the Institute of Atmospheric Physics, Chinese Academy of Sciences, Beijing, China, in 2013.

Her research interests mainly aimed at radiometric calibration and validation for infrared sensors.



Na Xu received the Ph.D. degree from the National Satellite Meteorological Center, China Meteorological Administration.

She is a Researcher, the Division Director of the National Satellite Meteorological Center, China Meteorological Administration, and also an assistant to the Chief Director of FengYun meteorological satellite project, the Deputy Chief Engineer of FengYun-3 composite satellite ground application system, was formerly the Chief Designer of FengYun geostationary and polar orbiting series satellite product generation system (PGS), responsible for FengYun-3 medium resolution spectral imager instrument (MERSI), was responsible for atmospheric precipitable water products and nocturnal cloud optical and microphysical products. She has long been engaged in research related to quantitative remote sensing of Fengyun meteorological satellites and has done a lot of work in the calibration and inversion of geophysical parameters, making outstanding contributions to promoting the improvement of remote sensing instrument process of Fengyun meteorological satellites, and the improvement of observation data quality and application capability of Fengyun optical remote sensors.



Danyu Qing received the Ph.D. degree in atmospheric physics and atmospheric environment from the Nanjing University of Information Science and Technology, Nanjing, China, in 2004.

He is currently the Chief Designer of the Fengyun Satellite Project Application System, China Meteorological Administration (CMA), and the Director of the International User Service Centre, National Satellite Meteorological Centre (NSMC). His research focuses on mesoscale convection activities, especially from the view of satellite. His research interests include satellite weather and remote sensing applications of Fengyun satellites.



Xiuqing Hu is the Senior Scientist (Grade 2) of National Satellite Meteorological Center, the Chief Designer of the Ground Segment and Application System for Fengyun-3 Meteorological Satellite and Chairman of the Research Group of WMO/GSICS. He has been leading the top-level design and development of the ground segment and application system for Fengyun-3 meteorological satellite for a long time, ever serving successively as the instrument scientist, and the Deputy Chief Designer. His research interests include high level design of newgeneration low-orbit meteorological satellite and requirement research; theory and technology method research on space-born instrument calibration; preprocessing and quality enhancement of remote sensing data; scientific inversion algorithms, and AI application of remote sensing big data.

newgeneration low-orbit meteorological satellite and requirement research; theory and technology method research on space-born instrument calibration; preprocessing and quality enhancement of remote sensing data; scientific inversion algorithms, and AI application of remote sensing big data.



Peng Zhang (Senior Member, IEEE) was born in Shannxi, China, in October 1970. He received the Ph.D. degree in atmospheric physics from the Institute of Atmospheric Physics, Chinese Academy of Sciences (IAP/CAS), Beijing, China in 1998.

He worked in Earth Observation Research Center, National Space Development Agency of Japan (EORC/NASDA) with a Post Doctor position from 1998 to 2001. He worked at National Satellite Meteorological Center, China Meteorological Administration (NSMC/CMA) from 2001 to 2023, and was the Deputy Director-General from 2013 to 2023. He was the Visiting Scholar at Centre de Meteorologie Spatiale, Meteo-France (CMS/Meteo-France) in 2003 and the Visiting Associate Scientist at Cooperative Institute for Meteorological Satellite Studies, Space Science and Engineering Center, University of Wisconsin-Madison (CIMSS/SSEC/UW-Madison) in 2005. He has been the Director-General of CMA Meteorological Observation Centre (MOC) since 2023. Currently, he is the Chief Scientist of Chinese polar-orbiting meteorological satellite program and his major fields cover the atmospheric remote sensing, instrument calibration and validation, and atmospheric radiative transfer calculation, etc.



Jing Li received the B.S. degree from Peking University, Beijing, China, in 2006, and the Ph.D. degree from Columbia University, New York, NY, USA, in 2011.

She is an Associate Professor with the Department of Atmospheric and Oceanic Sciences, School of Physics, Peking University. She has been working at Peking University since 2015. Her research interests focus on aerosol remote sensing and aerosol-climate interactions.



Xiaoxuan Mou received the bachelor's and master's degree from the China University of Geosciences (Wuhan), Wuhan, China, in 2018 and 2021, respectively.

Her research interests primarily revolve around algorithms for satellite observation.



Zijing Liu received a bachelor's degree from Nanjing University of Information Science and Technology in 2016, and received a Master's degree from Chinese Academy of Meteorological Sciences. He is currently working at the Guangdong Meteorological Bureau. He is mainly engaged in satellite remote sensing research.